

# Model-Based Estimation of Lithium Concentrations and Temperature in Batteries Using Soft-Constrained Dual Unscented Kalman Filtering

Stefano Marelli, Matteo Corno

**Abstract**—Safe and effective use of Lithium ion (Li-ion) batteries requires advanced Battery Management Systems (BMS). BMSs monitor the state of the battery (state-of-charge, state-of-power, temperature) and limit the current. The better the estimation of these internal states, the more energy the BMS is capable of safely extracting from the battery. The paper proposes an electrochemical model-based estimate of the Li-ion concentration and temperature of a cell. The use of the electrochemical approach allows not only for the estimation of the bulk State of Charge (SoC), but also for the estimation of the spatial distribution of lithium and temperature. The paper develops a soft-constrained Dual Unscented Kalman Filter (DUKF). The dual nature, along with parallelization, reduces the computational complexity; the soft-constraint improves accuracy and convergence. A thorough and realistic simulation analysis validates the approach showing bulk SoC estimation error lower than 1.5%, solid phase lithium concentration estimation errors of less than 4% in any point of the cell and temperature estimations errors within 0.2°C from the true value in any point of the cell.

**Index Terms**—Li-ion batteries, electrochemical-thermal model, Dual Unscented Kalman Filter, soft-constraint

## I. INTRODUCTION

LITHIUM ION (Li-ion) batteries are the most widely adopted technology for electric mobility and consumer electronics, thanks to their ability to store and deliver electric energy more efficiently and effectively than other chemistries. Unfortunately, Li-ion batteries are chemically unstable; they thus require Battery Management Systems (BMSs) to be safely operated [1], [2]. The BMS ensures safe operation by continuously monitoring: temperature, current, voltage, amount of remaining energy, and degradation. The BMS controls the current to avoid that any of the internal states of the battery exceed their safety limits, thus preventing damages and safety risks. Many of the internal states that need to be monitored cannot be directly measured; one of the key functions of the BMS is therefore to provide an estimate of these states. The more accurate this estimate is, the closer the battery can be exploited to its fundamental limits. If uncertainties or errors are present in the estimation, the BMS needs to adopt a conservative approach to avoid damaging the battery. For these reasons, state estimation is one of the key field in Li-ion BMS design.

A Li-ion cell is mainly composed of a negative and positive electrode, and a separator [3]. The electrodes have a lattice

structure in which lithium is stored; they are immersed in an (usually liquid) electrolyte. The separator allows only the lithium ions to flow through it, while it is an electrical insulator. During discharge, lithium diffuses to the surface of active material particles of the negative electrode and it undergoes the electron-generating reaction. Then, lithium ions dissolve in the electrolyte and cross the separator, while electrons are conducted to the current collector by the solid lattice. Eventually, both lithium ions and electrons reach the positive electrode and are reabsorbed in the active material particles. This process is called *dual-intercalation* [4] and is depicted in Figure 1.

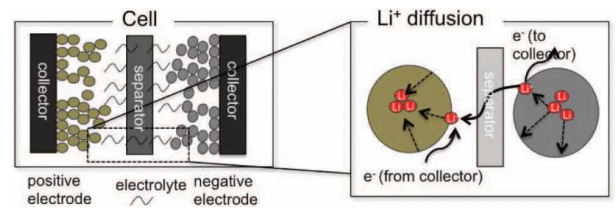


Fig. 1. Scheme of the dual-intercalation process in a Li-ion cell.

Several models of the Li-ion batteries exist. They are classified according to their complexity and accuracy (see for example [5]). The simplest models for Li-ion cells are the equivalent circuit models (ECMs) [6]–[8], or *gray-box* models. They describe the cells dynamics with minimum computational cost by means of elementary electric circuits with voltage sources, resistors and capacitors; these components may be given a (possibly non-linear) characteristic. These models are sufficiently accurate during low-current events; but they fail to describe the cell dynamics during high current events. First-principle electrochemical models, that describe the electrochemical reactions, overcome these limitations. Different first-principle modeling approaches exist: from rather simple Single Particle Models (SPM) [9] to advanced Computational Fluid Dynamics (CFD) models [10], that describe physical phenomena in all directions of the cell with extreme accuracy, but at the price of high computational burden and high number of electrochemical parameters to be identified. All these models may or may not include descriptions of the thermal dynamics. As for the dual intercalation dynamic models, thermal models exist at different levels of computational cost and accuracy [11]. For example, in [12] the authors develop a lumped thermal model for a cylindrical Li-ion cell, which lacks the effects of temperature state on the electrochemical dynamics.

In [3], [10], space-distributed electrochemical-thermal models are proposed, in which the influence of electrochemical and thermal parts is reciprocal.

The availability of an accurate electrochemical-thermal model and its incorporation in the BMS is critical for safe and effective use of Li-ion batteries. It is known [5] that for demanding current conditions, while averaged electrochemical quantities such as voltage ( $V$ ) and State of Charge (SoC) may reside in their safe region, a few areas in the electrodes may suffer of local conditions that are detrimental for the cell life and/or performance. In particular, using reactions overpotentials and lithium concentrations limitations rather than voltage limitations leads to improvements in terms of energy extraction and aging. This approach can only be implemented by employing a sufficiently accurate estimate, with insight on the electrochemical reactions taking place inside the cell. Internal lithium concentration distributions are a crucial information to effectively avoid reaching locally critical depletion levels [13]. In addition, it is shown in [14] that the electrochemical model dynamics are heavily affected by temperature. However, similarly to what happens for concentrations, large differences between surface and core temperatures can be generated during normal cell operation [12]. If one only monitors the surface temperature, which is the only thermal state that is measurable without altering the structural integrity of a cylindrical cell (*i.e.*, for example, without drilling a hole to measure the core temperature), a thermal runaway may not be promptly detected, thus leading to premature cell degradation or even to explosions [15]. As such, whilst a bulk thermal model may be enough to improve the electrochemical model accuracy, a knowledge of the temperature distribution is needed to prevent harmful and safety-critical conditions.

The Pseudo 2-Dimensional (P2D) electrochemical model, adopted in works such as [4], [16]–[20], is widely recognized as a valuable trade-off between detailed modeling and computational cost. However, this model, relying on Partial Differential Algebraic Equations (PDAEs), requires particular care in the implementation and in the observer formulation. Several methods are available in literature to find approximated and/or reduced-order solutions [21]–[23]. For instance, the diffusion dynamics in the spherical particles radial direction may be simplified: [24] assumes parabolic or polynomial concentrations distribution in active material particles. Integral expressions in short times and long times for the response of reaction molar flux were, instead, introduced by [16]. Moreover, [18] proposed an impedance model for solid phase diffusion, and applied Finite Elements Method (FEM) on electrolyte phase. In the present work, the P2D model is coupled with a distributed thermal model of a cylindrical Li-ion cell, as described in [25], and a Finite Difference Method (FDM) space-discretization technique is employed for the PDAEs, because it allows for easy order rescaling, while maintaining the physical meaning of all the variables and parameters.

The accuracy and the complexity of state estimation techniques is strictly related to that of the models they employ. A non-linear fractional order model, based on an ECM, is

employed by [26], and it is used for battery SoC estimation. One of the most outstanding approach employs the electrochemical SPM [27], but it neglects temperature dynamics. In [28] the authors adopt an approximated version of the SPM, and propose a way to compensate for model uncertainty and electrolyte dynamics simplification. Elsewhere, the P2D model is employed by proposing different approaches for order reduction: [13] estimates the instantaneous available current; [29] estimates the bulk SoC using an Extended Kalman Filter (EKF) on a space-discretized and reduced-order version of the P2D model; [19] estimates also the lithium concentrations using orthogonal collocation and a Kalman filter. The latter work includes a bulk thermal model of the cell. Better results may be obtained with a distributed thermal model, and with more advanced filtering techniques, given the highly non-linear nature of the cell electrochemical dynamics. The use of the Unscented Kalman Filter (UKF) [30] is investigated in [31] for SoC estimation in a simple ECM, while [32] applies it to a volume-averaged electrochemical model. These results prove that the UKF is an interesting tool to account for the cell non-linear electrochemical dynamics. In a previous work by the same authors of this manuscript [33], the application of the UKF is extended to the complete (*i.e.* not simplified) electrochemical P2D model. This work extends those results by proposing a Dual Unscented Kalman Filter (DUKF) algorithm, that encompasses both the P2D and a distributed thermal model. The dual observer structure is often exploited in the literature for state and parameter estimation, and in some works UKF is chosen as the estimator for such purposes [34]. Here, the proposed dual structure is instead dedicated to electrochemical and thermal states estimation; in particular, the DUKF consists in an UKF dedicated to lithium concentrations estimation, and an UKF dedicated to temperatures estimation. The former receives the estimated cell bulk temperature from the latter, while the latter receives the estimated concentrations from the former, thus accomplishing the coupling of the two parts of the DUKF. The proposed DUKF estimator has four main advantages:

- 1) It does not require a closed-form solution of the dynamics, thus avoiding the need to solve the algebraic constraints analytically or to numerically compute the Jacobian. An EKF implementation would require either operation.
- 2) It can easily accommodate to the inclusion of soft-constraints that improve the estimation convergence, as illustrated in the following.
- 3) It is prone to parallel implementation, as pointed out in [35].
- 4) While retaining the desired level of accuracy, it makes use of the minimal set of information, as discussed below.

Furthermore, here it is proven that the proposed DUKF approach is robust with respect to noisy voltage and surface temperature measurements; this consideration is not always reported in literature for other approaches (see, for example, [29] or [32]).

The main contributions of the present manuscript are sum-

marized as follows:

- 1) A DUKF is applied for the first time to lithium concentrations and local temperature estimation using the complete P2D model coupled to a distributed thermal model.
- 2) Estimation convergence issues with the complete P2D model are first investigated in simulation, then overcome by means of a *soft-constrained* formulation of the DUKF observer.
- 3) The DUKF observer is successfully implemented with a parallel computation approach, sensibly reducing its computational burden.

This paper is structured as follows. In Section II, the coupled electrochemical-thermal model is recalled, by summarizing the main characteristics of the P2D model and of the thermal model, highlighting the coupling terms, and applying the space-discretization to each part. In Section III, the concept of DUKF is first stated; then, the main problems arising from the UKF application to the P2D model are described, and subsequently overcome by implementing the concept of soft-constrained DUKF; also, the results of DUKF parallel implementation are presented. In Section IV, some DUKF tuning considerations are reported. The novel approach is fully validated in Section V, with also a remark on the validity of the proposed dual structure. In Section VI, conclusions are finally drawn.

## II. COUPLED ELECTROCHEMICAL-THERMAL MODEL

This section described the model used in designing the observer. The overall model is composed of two parts, namely the P2D electrochemical model and the thermal model, which are described separately here, for the sake of clarity. The P2D model describes the dynamics of the concentrations of lithium in the cell, and of all the quantities that depend algebraically on concentrations; the thermal model describes the temperature dynamics, driven by local heat generation mechanisms. These two parts exhibit bidirectional interactions, in that the electrochemical reactions are influenced by the temperature at which they take place, and the heat generation mechanisms depend on the values of electrochemical states. The interactions among the two parts are eventually described in this section as well, whereas a comment on how these interactions are dealt with in the proposed observer is provided in Section III.

### A. Pseudo-2-Dimensional electrochemical model

The P2D model describes the dual-intercalation process by a set of PDAEs. The only considered diffusion dynamics are those taking place across the battery film thickness, indicated as *longitudinal direction*  $x$ , and inside the spherical particles, along the *radial direction*  $r$ . The conservation equations are summarized in Table I. In these equations,  $c_s$  is the lithium concentration in solid phase;  $c_e$  is the Li-ion concentration in electrolyte phase;  $i_s$  is the electronic current in solid phase;  $i_e$  is the ionic current in electrolyte phase;  $\phi_s$  is the solid phase potential;  $\phi_e$  is the electrolyte phase potential.  $I$  is the cell current, which is the input of this model (assumed positive in

TABLE I  
ELECTROCHEMICAL MODEL - CONSERVATION PDAEs (BOUNDARY CONDITIONS ARE MARKED WITH GRAY BACKGROUND).

<b>Species: solid phase</b>
$\frac{\partial c_s}{\partial t} = \frac{D_s}{r^2} \frac{\partial}{\partial r} \left( r^2 \frac{\partial c_s}{\partial r} \right)$
$\frac{\partial c_s}{\partial r} \Big _{r=0} = 0$
$D_s \frac{\partial c_s}{\partial r} \Big _{r=R_s} = \frac{-j^{Li}}{a_s F}$
<b>Species: electrolyte phase</b>
$\frac{\partial \varepsilon_e c_e}{\partial t} = \frac{\partial}{\partial x} \left( D_e^{eff} \frac{\partial c_e}{\partial x} \right) + \frac{1-t_+^0}{F} j^{Li}$
$\frac{\partial c_e}{\partial x} \Big _{x=0} = 0$
$\frac{\partial c_e}{\partial x} \Big _{x=L} = 0$
<b>Charge: solid phase</b>
$i_s = -\sigma^{eff} \frac{\partial \phi_s}{\partial x}$
$\frac{\partial \phi_s}{\partial x} \Big _{x=\delta_n} = \frac{\partial \phi_s}{\partial x} \Big _{x=\delta_n+\delta_s} = 0$
$-\sigma^{eff} \frac{\partial \phi_s}{\partial x} \Big _{x=0} = -\sigma^{eff} \frac{\partial \phi_s}{\partial x} \Big _{x=L} = \frac{I}{A}$
<b>Charge: Electrolyte Phase</b>
$i_e = -k^{eff} \frac{\partial \phi_e}{\partial x} - k_D^{eff} \frac{\partial \ln(c_e)}{\partial x}$
$\frac{\partial \phi_e}{\partial x} \Big _{x=0} = 0$
$\frac{\partial \phi_e}{\partial x} \Big _{x=L} = 0$

discharge). Also,  $D_s$  is the solid phase diffusion coefficient;  $F$  is Faraday's constant;  $a_s$  is the electrode specific interfacial area;  $D_e^{eff}$  is the effective diffusion coefficient;  $t_+^0$  is Li-ion transference number (assumed as a constant);  $\sigma^{eff}$  is the effective conductivity;  $k^{eff}$  is the effective ionic conductivity, while  $k_D^{eff}$  is the effective diffusion conductivity. Finally, a few geometrical quantities are defined as well:  $A$  is the electrode plate area;  $\delta_{n,p,s}$ , are, respectively, the negative and positive electrodes and separator thicknesses;  $L = \delta_n + \delta_p + \delta_s$  is the overall film thickness;  $R_s$  is the radius of the active material spherical particles.

The *Butler-Volmer kinetics* equation describes the molar flux  $j^{Li}$  at the active material particles surface:

$$j^{Li} = a_s j_0 \left[ \exp \left( \frac{\alpha_a F}{RT} \eta \right) - \exp \left( -\frac{\alpha_c F}{RT} \eta \right) \right] \quad (1)$$

where  $\alpha_{a,c}$  are, respectively, the anodic and cathodic transfer coefficients;  $R$  is the universal gas constant;  $T$  is the temperature at which the reaction takes place;  $j_0$  is the exchange current density. The reaction overpotential  $\eta$  is defined as:

$$\eta = \phi_s - \phi_e - U(c_{se}) \quad (2)$$

where  $U$  is the thermodynamic equilibrium potential and is a non-linear function of the surface concentration  $c_{se}$  [17]. The

gradients of  $i_s$  and  $i_e$  along  $x$  are related to  $j^{Li}$  as follows:

$$\frac{\partial i_s}{\partial x} = -j^{Li}, \quad \frac{\partial i_e}{\partial x} = j^{Li}. \quad (3)$$

Equations (3) are subject to the following constraints inside the separator  $x \in [\delta_n, \delta_n + \delta_s]$ :

$$\begin{aligned} \frac{\partial i_s}{\partial x}(x) &= \frac{\partial i_e}{\partial x}(x) = 0 \\ i_s(x) &= 0 \\ i_e(x) &= \frac{I}{A}. \end{aligned}$$

Finally, the terminal cell voltage is given by:

$$V = \phi_s(x=L) - \phi_s(x=0) - \frac{R_f}{A} I \quad (4)$$

where  $R_f$  is the electrode surface film resistance. In the following, the cell parameters proposed and experimentally identified in [17] are adopted.

The coupling with the thermal part of the model takes place through the term  $T$  appearing explicitly in (1). Also, a few parameters of the P2D model are considered temperature-dependent; more specifically, these are: the exchange current density  $i_0$ , the diffusion coefficient in the solid phase  $D_s$ , the diffusion coefficient in the electrolyte phase  $D_e$  and the electrolyte ionic conductivity  $k$ . All these parameters depend on the temperature according to the Arrhenius equation:

$$\Psi(T) = \Psi_{ref} \left[ \frac{E_{act}^\Psi}{R} \left( \frac{1}{T_{ref}} - \frac{1}{T} \right) \right]$$

where  $\Psi$  is the generic parameter among those considered,  $\Psi_{ref}$  is the value of the parameter at the reference temperature  $T_{ref} = 25^\circ\text{C}$ ,  $E_{act}^\Psi$  is the activation energy for the parameter  $\Psi$ .

Given the above model, the stoichiometry  $\theta_s$  is defined as the ratio between the local value of concentration  $c_s$  and its maximum value  $c_{s,max}$  [17]; and  $\theta_{se}$  is the stoichiometry evaluated at an active material particle surface. SoC is defined as the average stoichiometry in negative electrode [4], normalized between two experimentally determined limits [29]:

$$\text{SoC} = \frac{\left( \frac{3}{\delta_n R_s^3} \int_0^{\delta_n} \int_0^{R_s} r^2 \theta_s \, dr dx \right) - \theta_{s,0\%}}{\theta_{s,100\%} - \theta_{s,0\%}} \quad (5)$$

where  $\theta_{s,0\%}$  is the limit stoichiometry at SoC = 0%, and  $\theta_{s,100\%}$  is the limit stoichiometry at SoC = 100%. SoC is synthetically representative for the amount of charge available inside the cell.

The FDM approach is used to space-discretize the P2D model, as depicted in Figure 2. The cell is discretized along  $x$  in  $N_{n,p,s}$  elements, respectively for the negative and positive electrodes, and the separator; each element occupies a space  $\Delta x_{n,p,s}$ , respectively. Inside each electrode there is a number of active material spherical particles equal to the ratio between the effective electrode volume and the volume of a single sphere:

$$\nu_{n,p} = \frac{\delta_{n,p}}{\frac{4}{3}\pi R_s^3} A \varepsilon_{s;n,p}$$

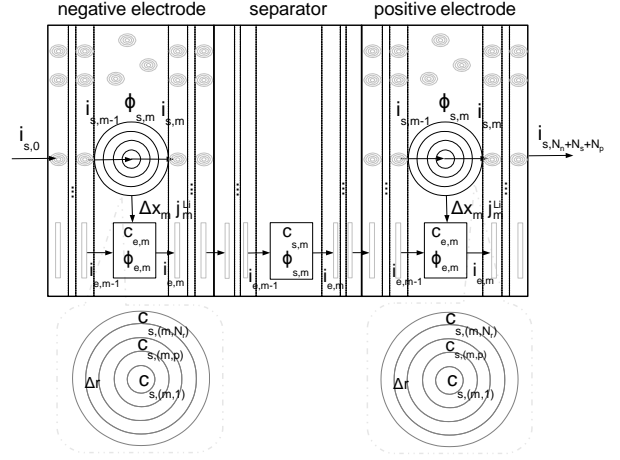


Fig. 2. Discretization of Li-ion cell along the  $x$  and  $r$  directions.

where  $\varepsilon_{s;n,p}$  is the solid phase volume fraction of negative and positive electrodes, respectively. As such, in each discretized element of the electrodes there is a number of spherical particles respectively equal to:

$$\nu_{n,p}^{\Delta x} = \frac{V_{n,p}}{N_{n,p}}$$

Each active material spherical particle is further discretized along its radius  $r$  in  $N_r$  elements, spaced  $\Delta r$ . Since all equations are written with volume-specific quantities, there is no need to consider all the  $\nu_{n,p}^{\Delta x}$  spheres for each discretized element, but just one sphere is representative also for the dynamics of all the others within the same element. Overall, the electrochemical model is described by  $(N_r+1)(N_n+N_p)+N_s$  Ordinary Differential Equations (ODEs), plus  $5(N_n+N_p)+2N_s-3$  non-linear algebraic constraints.

The conservation equations for the resulting discretized model are summarized in Table II, in the form of Differential Algebraic Equations (DAEs). In the table and in the following, index  $m$  is used for discretized elements along  $x$  and index  $p$  for discretized elements along  $r$ . The Butler-Volmer kinetics equation (1) becomes:

$$j_m^{Li} = a_s j_0 \left[ \exp\left(\frac{\alpha_a F}{RT} \eta_m\right) - \exp\left(-\frac{\alpha_c F}{RT} \eta_m\right) \right]$$

and overpotential (2) is written as:

$$\eta_m = \phi_{s,m} - \phi_{e,m} - U(c_{s,(m,N_r)}).$$

Furthermore, the relations involving molar flux (3) become, respectively:

$$i_{s,m} - i_{s,m-1} = -\Delta x_m j_m^{Li}, \quad i_{e,m} - i_{e,m-1} = \Delta x_m j_m^{Li}.$$

The cell output equation (4) is written as:

$$V = \phi_{s,N_n+N_s+N_p} - \phi_{s,1} - \frac{R_f}{A} I.$$

Finally, SoC (5) is computed as:

$$\text{SoC} = \frac{1}{N_n R_s^3} \sum_{m=1}^{N_n} \sum_{p=1}^{N_r} c_{s,(m,p)} (r_p^3 - r_{p-1}^3)$$

TABLE II  
DISCRETIZED ELECTROCHEMICAL MODEL - CONSERVATION DAES  
(BOUNDARY CONDITIONS ARE MARKED WITH GRAY BACKGROUND).

Species: solid phase
$\dot{c}_{s,(m,p)} = \frac{D_s}{(p\Delta r)^2} \left[ 2p\Delta r \left( \frac{c_{s,(m,p+1)} - c_{s,(m,p)}}{\Delta r} \right) + (p\Delta r)^2 \left( \frac{c_{s,(m,p-1)} - 2c_{s,(m,p)} + c_{s,(m,p+1)}}{\Delta r^2} \right) \right]$
$c_{s,(m,1)} - c_{s,(m,0)} = 0$
$D_s \left( \frac{c_{s,(m,N_r+1)} - c_{s,(m,N_r)}}{\Delta r} \right) = \frac{-j_m^{Li}}{a_s F}$
Species: electrolyte phase
$\dot{c}_{e,m} = \frac{D_e^{eff}}{\varepsilon_e} \left( \frac{c_{e,m-1} - 2c_{e,m} + c_{e,m+1}}{\Delta x_m^2} \right) + \frac{1-t_+^0}{F\varepsilon_e} j_m^{Li}$
$c_{e,1} - c_{e,0} = 0$
$c_{e,N_n+N_s+N_p+1} - c_{e,N_n+N_s+N_p} = 0$
Charge: solid phase
$i_{s,m} = -\sigma^{eff} \left( \frac{\phi_{s,m+1} - \phi_{s,m}}{\Delta x_m} \right)$
$i_{s,N_n} = i_{s,N_n+N_s} = 0$
$i_{s,0} = i_{s,N_n+N_s+N_p} = \frac{I}{A}$
Charge: Electrolyte Phase
$i_{e,m} = -k^{eff} \left( \frac{\phi_{e,m+1} - \phi_{e,m}}{\Delta x_m} \right) - k_D^{eff} \left( \frac{\ln(c_{e,m+1}) - \ln(c_{e,m})}{\Delta x_m} \right)$
$\phi_{e,1} - \phi_{e,0} = 0$
$\phi_{e,N_n+N_s+N_p+1} - \phi_{e,N_n+N_s+N_p} = 0$

where  $r_p$  is the radius of the  $p$ -th discretized element, equal to  $p\Delta r$ .

As an example of the electrochemical model capabilities, in Figure 3 the surface stoichiometry is reported along  $x$  at different time snapshots for a dynamic current input that will be described later (second scenario of Section V), while in Figure 4 the stoichiometry is reported along  $r$  inside a spherical particle located at  $x = L$ . The P2D model is

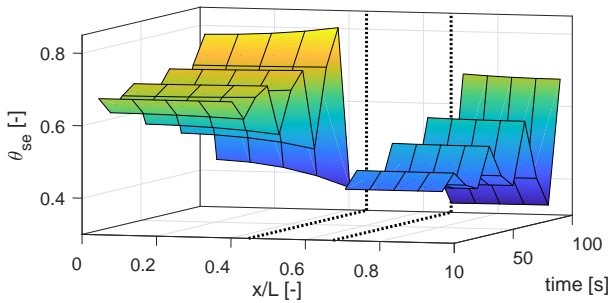


Fig. 3. Solid phase stoichiometry gradients during first 100s of the second scenario described in Section V: surface stoichiometry gradients along  $x$  direction. Dotted lines indicate the separation among domains: negative electrode (left), separator (center) and positive electrode (right).

discretized with  $N_r = 50$  and  $N_n = N_s = N_p = 5$ . It is clear how inner concentration gradients arise during normal cell cycling (both along  $x$  and  $r$  directions); as such,

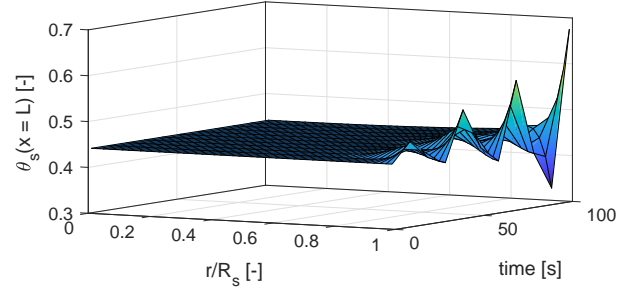


Fig. 4. Solid phase stoichiometry gradients during first 100s of the second scenario described in Section V: stoichiometry gradients along  $r$  direction.

the importance of an estimator capable of capturing these gradients is evident.

### B. Thermal model

The thermal model describes heat generation mechanisms by means of PDEs. It assumes that the temperature gradient along the cylinder *axial direction*  $y$  is negligible (see [36], [37]); thus, the temperature dynamics are those of heat conduction along the radius of a cylinder:

$$\rho c_p \frac{\partial T}{\partial t} = k_t \frac{\partial^2 T}{\partial r^2} + \frac{k_t}{r^c} \frac{\partial T}{\partial r^c} + Q \quad (6)$$

subject to boundary conditions:

$$\left. \frac{\partial T}{\partial r^c} \right|_{r^c=0} = 0, \quad \left. \frac{\partial T}{\partial r^c} \right|_{r^c=R^c} = -\frac{h}{k_t} (T - T_\infty) \quad (7)$$

where  $T_\infty$  is the environment temperature (considered constant here),  $k_t$  is the thermal conductivity,  $\rho$  is the density,  $h$  is the convection heat transfer coefficient,  $c_p$  is the specific heat capacity,  $Q$  is the volumetric heat generation rate,  $r^c$  is the *radial direction* and  $R^c$  is the radius of the cylinder. Since the cylinder is a heterogeneous domain, being composed of two different phases (solid and electrolyte) distributed in three domains (negative electrode, positive electrode and separator), the heat capacity  $C_p$  is computed as in [38]:

$$C_p = \rho c_p = \sum_{i,k} \frac{\delta_i \varepsilon_{k,i} \rho_{k,i} c_{p,k,i}}{L}$$

where subscript  $k = (s, e)$  indicates the phase (solid or electrolyte) and subscript  $i = (n, s, p)$  indicates the component.  $Q$  is the sum of three terms: the volumetric reaction heat  $Q_j$ , the volumetric ohmic heat  $Q_o$  and the volumetric contact resistance heat  $Q_f$ :

$$Q = Q_j + Q_o + Q_f \quad (8)$$

where:

$$\begin{aligned} Q_j &= \frac{1}{L} \int_0^L j^{Li} \eta dx \\ Q_o &= \frac{1}{L} \int_0^L \sigma^{eff} \left( \frac{\partial \phi_s}{\partial x} \right)^2 + k^{eff} \left( \frac{\partial \phi_e}{\partial x} \right)^2 \\ &\quad + k_D^{eff} \left( \frac{\partial \ln(c_e)}{\partial x} \right) \left( \frac{\partial \phi_e}{\partial x} \right) dx \\ Q_f &= \frac{R_f}{L} \left( \frac{I}{A} \right)^2. \end{aligned} \quad (9)$$

The input to this part of the model is again the cell current  $I$ . The measured output is the cell surface temperature  $T_{surf}$ , because no other temperature measurement is available, as observed above. The experimentally identified cell parameters proposed in [14], [39] are adopted in the following.

The coupling with the electrochemical part of the model takes place through volumetric heats  $Q_j$  and  $Q_o$ , that depend on several electrochemical algebraic variables, and thus on the electrochemical states.

Also in this case, the model PDEs are discretized using the FDM, as depicted in Figure 5. The cell is discretized along

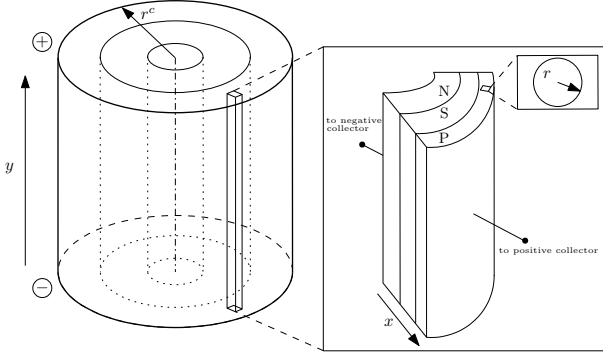


Fig. 5. Discretization of Li-ion cell along the  $r^c$  direction.

$r^c$  in  $N_c$  elements, using a constant-volume approach. This means that all the  $N_c$  subcells have the same volume, and the resulting radial increment is not uniform.

The temperature dynamics (6) become:

$$\rho c_p \dot{T}_z = k_t \left[ \frac{T_{z-1} - 2T_z + T_{z+1}}{(\Delta r_z^c)^2} \right] + \frac{k_t}{r_z^c} \left[ \frac{T_{z+1} - T_z}{\Delta r_z^c} \right] + Q_z \quad (10)$$

which is a set of  $N_c$  ODEs. Boundary conditions (7) are formulated as:

$$T_1 - T_0 = 0, \quad \frac{T_{N_c+1} - T_{N_c}}{\Delta r_{N_c}^c} = -\frac{h}{k_t} (T_{N_c} - T_\infty).$$

In the equations above, index  $z$  is used for discretized elements along  $r^c$ . The radial increment  $\Delta r_z^c$  is the space occupied by the  $z$ -th subcell; it is defined as:

$$\Delta r_z^c = r_z^c - r_{z-1}^c.$$

Given that the entire volume of the cell is divided into  $N_c$  subcells, each characterized by its own temperature, the electrochemical model described in Subsection II-A should be specific for each subcell. This gives a total of  $N_c [(N_r + 1)(N_n + N_p) + N_s] + N_c$  states for the discretized coupled electrochemical-thermal model. Also, since the current collector is a common element of all subcells, they are all connected in parallel; this means that they exhibit the same terminal voltage. Thus, an additional set of algebraic constraints arises, of the form:

$$V_z - V_{z-1} = 0, \quad \text{with } z \in [2, N_c]. \quad (11)$$

In total, there are  $N_c [5(N_n + N_p) + 2N_s - 3] + N_c - 1$  algebraic constraints. By discretizing (8) and (9), the volumetric

heat generation rate and the individual heat terms become, respectively:

$$Q_z = Q_{j,z} + Q_{o,z} + Q_{f,z}$$

and

$$\begin{aligned} Q_{j,z} &= \frac{1}{L} \sum_m j_{m,z}^{Li} \eta_{m,z} \Delta x_m \\ Q_{o,z} &= \frac{1}{L} \sum_m \left[ \sigma^{eff} \left( \frac{\phi_{s,m+1,z} - \phi_{s,m,z}}{\Delta x_m} \right)^2 \right. \\ &\quad + k^{eff} \left( \frac{\phi_{e,m+1,z} - \phi_{e,m,z}}{\Delta x_m} \right)^2 \\ &\quad + k_D^{eff} \left( \frac{\ln(c_{e,m+1,z}) - \ln(c_{e,m,z})}{\Delta x_m} \right) \\ &\quad \left. \cdot \left( \frac{\phi_{e,m+1,z} - \phi_{e,m,z}}{\Delta x_m} \right) \right] \Delta x_m \\ Q_{f,z} &= \frac{R_f}{L} \left( \frac{I_z}{A_z} \right)^2. \end{aligned}$$

The term  $I_z$  is the input current to the  $z$ -th subcell (a fraction of the total input current  $I$ ), while  $A_z$  is the subcell electrode plate area. Finally,  $T_{bulk}$  is computed as:

$$T_{bulk} = \frac{1}{Vol} \sum_{z=1}^{N_c} Vol_z T_z \quad (12)$$

where  $Vol$  is the total cell volume and  $Vol_z$  is the  $z$ -th subcell volume.

An example of the thermal model capabilities is shown in Figure 6. The temperature is reported along  $r^c$  at different time snapshots for the same current input as Figures 3 and 4. The thermal model is discretized with  $N_c = 6$ . The figure

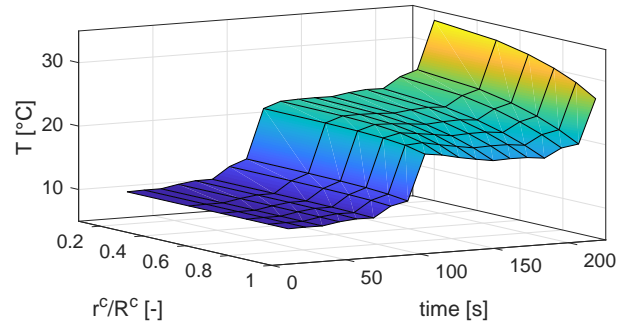


Fig. 6. Temperature gradients along  $r^c$  direction during first 225s of the second scenario described in Section V.

shows that a 10 degrees gradient builds up over 200 s. This test stresses the importance of an estimator capable of capturing temperature gradients during normal cell cycling, as is even better motivated in Subsection V-A.

### III. SOFT-CONSTRAINED DUAL UNSCENTED KALMAN FILTER ESTIMATOR

In this section, the structure of a standard UKF is first recalled, and then extended to the DUKF estimator. The advantages of the proposed dual structure are discussed. State estimation convergence issues in electrochemical UKF

formulation are studied in simulation and solved by means of a *soft-constraint* in Subsection III-A. Finally, a substantial improvement in computational time is obtained with a parallel implementation of the DUKF in Subsection III-B.

The UKF is a Sigma-Point Kalman Filter (SPKF) with a particular choice of weighting coefficients. In [30], details on UKF formulation and implementation are described, together with considerations on theoretical aspects. In summary, the UKF is a model-based estimator for non-linear dynamic systems, which presents several advantages compared to other Kalman-based estimators, including EKF:

- 1) the numeric/analytic computation of Jacobians is not required;
- 2) the computational cost is similar to that of EKF; and
- 3) in turn, accuracy of statistical moments estimation is of the third order for Gaussian systems [40].

The UKF algorithm is reported in Algorithm 1, for the case with additive process and measurement noises, indicated respectively with  $\xi$  and  $v$ . A set of *sigma-points* is deterministically sampled starting from the previous-step a-posteriori state estimate and covariance matrix. In the *time-update* step, each of these points is propagated through the system non-linear state equation; the results are then properly weighted to generate the current step a-priori state estimate and covariance matrix. Also, a-priori sigma-points are passed through the system non-linear output equation, and then properly weighted to give an estimate of the output and of its covariance matrix. Furthermore, the state and output cross-covariance matrix is estimated. Finally, in the *measurement-update* step, the Kalman gain is applied to the difference between the actual and estimated output, in order to compute the current-step a-posteriori state estimate and covariance matrix. It can be observed that the time-update step of the algorithm, and in particular (13) and (14), is naturally amenable to parallel computing implementation; in fact, each a-priori sigma-point computation, starting from  $\hat{x}_{k-1}^+$  and  $P_{xx,k-1}^+$ , is completely independent from other sigma-points.

If  $n_x$  is the dimension of the state vector, the sigma-points are in the number of  $2n_x + 1$ . The covariance matrix  $P_{xx,0}^+$  of the initial state estimate is a tuning parameter, which rules the initial dispersion of the sigma-points around the initial state estimate  $\hat{x}_0^+$ , that is another tuning parameter. The covariance matrix  $Q_{\xi\xi}$  of the process disturbance and the covariance matrix  $R_{vv}$  of the measurement noise are also important tuning parameters, as well as the other, minor tuning parameters, such as  $\alpha$ ,  $\beta$  and  $\kappa$ .

In the present work, the structure of UKF is exploited twice, so as to obtain the Dual Unscented Kalman Filter depicted in Figure 7. In this approach, the overall observer is composed of two parts: the electrochemical UKF and the thermal UKF. The electrochemical UKF includes only the P2D model of the cell. It receives as inputs the current and the estimated bulk temperature,  $\hat{T}_{bulk}$ , which comes from the thermal part of the observer; it receives the terminal voltage as the measured quantity (in the standard approach - see Subsection III-A for a deeper analysis on this); finally, it provides estimates of all discretized elements of  $c_s$  and  $c_e$ , gathered in the estimated state vector  $\hat{c}$ , and of the state of

---

**Algorithm 1** Unscented Kalman Filter for a system affected by additive process and measurement disturbances.

---

0: Non-linear state-space model:

$$\begin{aligned} x_k &= f(x_{k-1}, u_{k-1}, k-1) + \xi_{k-1} \\ y_k &= h(x_k, u_k, k) + v_k \end{aligned}$$

Definitions:

$$\begin{aligned} n_{sp} &= 2n_x + 1 \\ \lambda &= \alpha^2(n_x + \kappa) - n_x \\ w_{s,1} &= \frac{\lambda}{n_x + \lambda} \\ w_{c,1} &= \frac{\lambda}{n_x + \lambda} + 1 - \alpha^2 + \beta \\ w_{s,2:n_{sp}} &= w_{c,2:n_{sp}} = \frac{1}{2(n_x + \lambda)} \end{aligned}$$

1: Initialization:

$$\begin{aligned} \hat{x}_0^+ &= E[x_0] \\ P_{xx,0}^+ &= E[(x_0 - \hat{x}_0^+)(x_0 - \hat{x}_0^+)^T] \end{aligned}$$

2: Cycle for  $k = 1, 2, \dots$

Time-update:

$$\mathcal{X}_{k-1}^+ = \begin{bmatrix} \hat{x}_{k-1}^+ \\ \hat{x}_{k-1}^+ + \sqrt{(n_x + \lambda)P_{xx,k-1}^+} \\ \hat{x}_{k-1}^+ - \sqrt{(n_x + \lambda)P_{xx,k-1}^+} \end{bmatrix} \quad (13)$$

$$\mathcal{X}_{k,i}^- = f(\mathcal{X}_{k-1,i}^+, u_{k-1}, k-1) \quad (14)$$

$$\hat{x}_k^- = \sum_{i=1}^{n_{sp}} w_{s,i} \mathcal{X}_{k,i}^- \quad (15)$$

$$P_{xx,k}^- = \sum_{i=1}^{n_{sp}} w_{c,i} (\mathcal{X}_{k,i}^- - \hat{x}_k^-) (\mathcal{X}_{k,i}^- - \hat{x}_k^-)^T + Q_{\xi\xi}$$

$$\mathcal{Y}_{k,i} = h(\mathcal{X}_{k,i}^-, u_k, k)$$

$$\hat{y}_k = \sum_{i=1}^{n_{sp}} w_{s,i} \mathcal{Y}_{k,i}$$

$$P_{yy,k} = \sum_{i=1}^{n_{sp}} w_{c,i} (\mathcal{Y}_{k,i} - \hat{y}_k) (\mathcal{Y}_{k,i} - \hat{y}_k)^T + R_{vv}$$

$$P_{xy,k} = \sum_{i=1}^{n_{sp}} w_{c,i} (\mathcal{X}_{k,i}^- - \hat{x}_k^-) (\mathcal{Y}_{k,i} - \hat{y}_k)^T$$

$$K_k = P_{xy,k} P_{yy,k}^{-1}$$

Measurement-update:

$$\begin{aligned} \hat{x}_k^+ &= \hat{x}_k^- + K_k (y_k - \hat{y}_k) \\ P_{xx,k}^+ &= P_{xx,k}^- - K_k P_{yy,k} K_k^T \end{aligned} \quad (16)$$


---

charge. The dimension of the state for the electrochemical part of DUKF is  $n_x = (N_r + 1)(N_n + N_p) + N_s$ . On the other hand, the thermal UKF includes only the thermal model of the cell, and assumes all the  $N_c$  subcells to be characterized by the same electrochemical states  $c_s$  and  $c_e$  (distributed along  $x$  and  $r$ ). It receives as inputs the current and the estimated concentrations vector, which comes from the electrochemical part of the observer; it receives the surface temperature as the measured quantity; finally, it provides estimates of the temperatures of all the subcells, gathered in the estimated state vector  $\hat{T}$ . The dimension of the state for the thermal part of DUKF is  $n_x = N_c$ . The validity of the proposed structure is discussed in Subsection V-A.

From the computational efficiency standpoint, the proposed structure offers two main advantages:

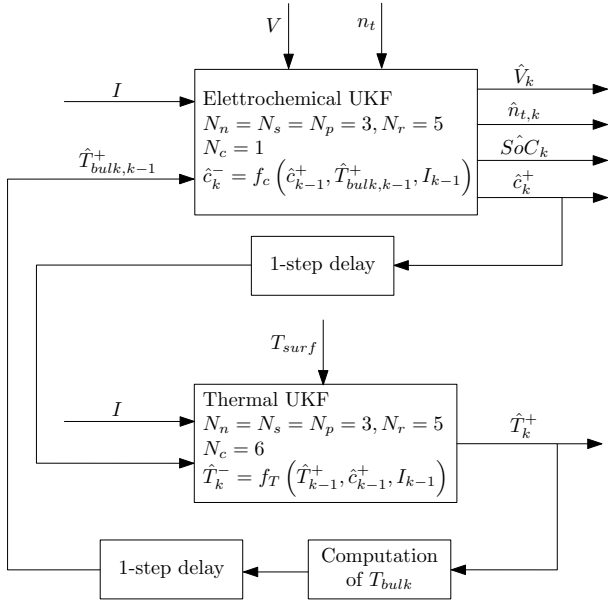


Fig. 7. Scheme of the Dual Unscented Kalman Filter estimator. The meaning of the signal  $n_t$  is explained in Subsection III-A.

- 1) It automatically solves the problem of the parallel configuration for the subcells. Instead of implementing the algebraic constraints (11), as is done in the coupled electrochemical-thermal simulator, the measured quantity  $V$  is forced to be the same for all the subcells through the assumption that all the subcells have the same electrochemical state  $c$ .
- 2) Compared to a full-order UKF with both electrochemical and thermal models in a monolithic observer, which would not be a practical solution due to excessive computational time, it is much more computationally manageable. In fact, while still retaining the capability of estimating both concentrations and temperature gradients, and showing high accuracy, it makes use of the minimal set of information. From extensive simulation studies, as those reported in Section V, it is observed that a bulk estimate of temperature is enough for the electrochemical part of the observer to accurately estimate lithium concentrations in any point of the cell. Similarly, assuming concentrations are equal among all discretized subcells is enough for the thermal part of the observer to correctly estimate the values of temperature along the cylinder radial direction.

#### A. Convergence issues with the electrochemical UKF implementation

It is well known that the lithium concentration is difficultly estimated from terminal voltage and current measurements. [41] and [27] discuss the lack of observability for the standard formulation of the SPM. [42] reaches the same conclusion by looking at the Jacobian of the Lie derivative of a reduced-order SPM with addition of electrolyte phase concentrations dynamics. The analytical analysis of the observability of the P2D model is made complex by its strong non-linearities and

coupled terms. However, a simple simulation study confirms the same problem. In this test, the current pulses cycle presented in Figure 8 is applied to the cell. The standard UKF

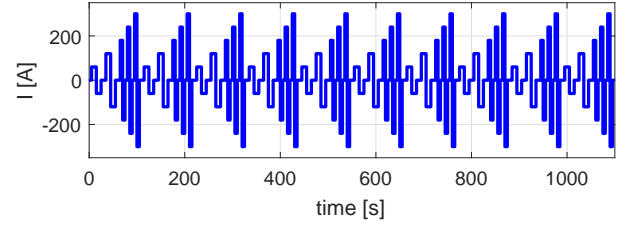


Fig. 8. Convergence issues with the standard application of UKF to SoC estimation: input current profile.

is applied to the discretized P2D model, with  $N_r = 5$  and  $N_n = N_s = N_p = 3$ , and with 5% initial SoC error for the estimator (note that this value is deliberately chosen as small). This analysis focuses only on the electrochemical part of the observer, because this is the only one involved in convergence issues. Figure 9 clearly shows that, while the terminal voltage estimation error converges to zero, the bulk SoC estimation error does not tend to 0.

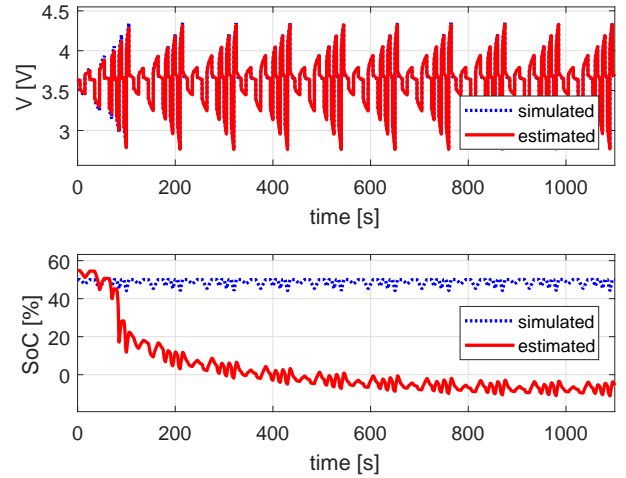


Fig. 9. Convergence issues with the standard application of UKF to SoC estimation (top: simulated and estimated terminal voltage; bottom: simulated and estimated SoC).

Figure 10 provide an interpretation of the issue; it plots the actual and estimated (by using the estimated concentrations) total number of moles of lithium available in the cell  $n_t$ . This

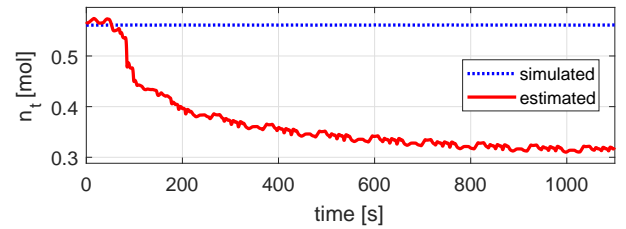


Fig. 10. Convergence issues with the standard application of UKF to SoC estimation: conservation of total lithium moles in solid phase, under the current profile of Figure 8.

is defined as the sum of the total number of moles of lithium

in solid phase  $n_s$  (which is the integral of  $c_s$  in the whole cell volume, i.e. both along  $r$  and along  $x$ , weighted by the solid phase volume fraction  $\varepsilon_s$ ) and the total number of moles of lithium in electrolyte phase  $n_e$  (which is the integral of  $c_e$  along  $x$ , weighted by the electrolyte phase volume fraction  $\varepsilon_e$ ):

$$\begin{aligned} n_s &= \frac{3A}{R_s^3} \int_0^L \int_0^{R_s} \varepsilon_s r^2 c_s dr dx \\ n_e &= A \int_0^L \varepsilon_e c_e dx \\ n_t &= n_s + n_e. \end{aligned} \quad (17)$$

Note that  $n_t$  is constant for a given cell, and it is directly computable from known model parameters. The results prove that the unscented estimation mechanism does not guarantee the conservation of the total number of moles of available lithium, or, equivalently, the conservation of total lithium mass. As a matter of fact, although the single sigma-point transformation through the model state equation (14) conserves the total lithium mass, being based on the P2D model formulation, a few other steps in the UKF algorithm do not provide the same feature. More in detail, the steps possibly altering the total lithium mass because of their purely statistical nature are: 1) sigma-points computation based on previous step a-posteriori state estimation and covariance matrix (13); 2) a-priori state estimation via weighted sum of sigma-points (15); 3) a-posteriori state estimation via measurement correction step (16). Thus, there are 3 specific mechanisms in the UKF algorithm that are unable to guarantee mass conservation. This causes the divergence of the estimate.

The structure of the electrochemical UKF is modified to account for the conservation of lithium, and improve convergence. One could adopt two approaches: a *hard-constraint* approach, adding additional algebraic constraints in the sigma-points computation; or a *soft-constraint* approach. The latter idea consists in modifying the input-output structure of the model by adding a *virtual* measurement, namely the total number of moles of available lithium  $n_t$  (constant signal). Thus, in Algorithm 1 it holds:

$$y = \begin{bmatrix} V \\ n_t \end{bmatrix}$$

where  $n_t$  can be computed with (17) starting from the knowledge of the cell physical parameters only. In fact, one can fix SoC at an arbitrary value, and compute the corresponding values of  $c_s$  and  $c_e$  at steady-state in the whole cell (i.e. in any point along  $x$  and  $r$ ), by inverting (5). In the electrochemical UKF tuning, the additive measurement noise variance corresponding to  $n_t$  is set to a value that is much smaller than that corresponding to  $V$ . Consequently, a *soft-constraint* is enforced in the estimator for the conservation of  $n_t$ , and the electrochemical model observability is effectively enhanced.

### B. Implementation with parallel computing

Each sigma-point propagation through the non-linear state equation takes place independently from other sigma-points;

this structure is thus suitable for parallel computing implementation. Most of the time-update step computational cost (i.e. the one due to the propagation of the sigma points) can be distributed on multiple cores and optimized, so that the time required for this step is ultimately significantly reduced.

The following computational cost analysis quantitatively illustrates this advantage. The dual estimator is run on the first 100s of the experiment shown in Figure 11. It consists

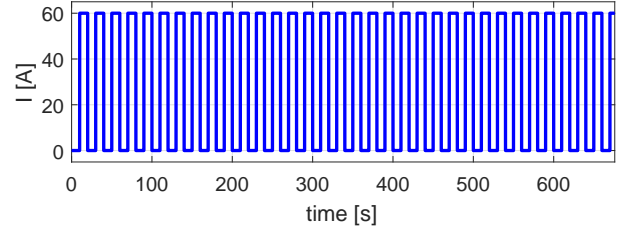


Fig. 11. Current input profile used to analyze computational cost: pulses sequence at 0-10C.

of a sequence of pulses at 10C followed by rest periods, both of 10s duration. Simulations were run in MathWorks MATLAB, with Parallel Computing Toolbox, on a quad-core machine (2.4GHz) with 12GB RAM and solid-state drive. The ratio between the simulation time required by the sequential and parallel implementation, respectively called  $T_{sim}^{seq}$  and  $T_{sim}^{par}$ , is shown in Figure 12, as a function of  $N_r$ , with  $N_n = N_s = N_p = 3$  and  $N_c = 6$ . By observing the

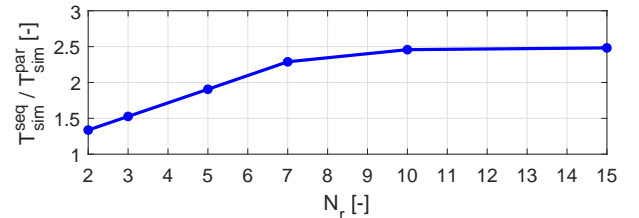


Fig. 12. Ratio between simulation time required by sequential and parallel computing implementation of UKF estimator, for different discretization levels  $N_r$ .

figure, it is clear that the estimation algorithm computational burden is reduced by a factor between 1.3 to 2.5 thanks to the parallel implementation. Note that, on a quad-core machine, a reduction by exactly a factor 4 is not practically possible, because of two reasons:

- the observer dual algorithm is not fully parallelizable, because the electrochemical and thermal parts act on distinct sets of sigma points;
- some computing overhead is introduced by the Parallel Computing Toolbox in order to manage the exchange of information among multiple solvers.

## IV. FILTER TUNING ANALYSIS

This section summarizes the results of the DUKF tuning procedure. The current input profile selected for this purpose is that of Figure 11. The simulation stops when the output voltage reaches the lower cutoff value of 2.7V; SoC is roughly 18% at the end of simulation, because it is not a quasi-static test. The

simulator is starting from  $\text{SoC} = 100\%$  and  $T = 10^\circ\text{C}$ , while the estimator is initialized at  $\text{SoC} = 80\%$  and  $T = 20^\circ\text{C}$ . Ambient temperature is kept at  $T_{amb} = 10^\circ\text{C}$  to simulate an active cooling system acting on the cell. The observer is based on the following discretization:  $N_r = 5$ ,  $N_n = N_s = N_p = 3$  and  $N_c = 6$ . Covariance matrices are all chosen as diagonal matrices, and designed as follows (subscript  $c$  stands for the electrochemical UKF, and  $T$  stands for the thermal UKF):

- the covariance matrix  $P_{xx,c,0}^+$  of the initial state estimate has elements on the main diagonal equal to  $p_{cs}$  for lines in the state vector corresponding to  $c_s$  and  $p_{ce}$  for lines corresponding to  $c_e$ ; the covariance matrix  $P_{xx,T,0}^+$  has elements on the main diagonal equal to  $p_T$  for lines corresponding to  $T$ ;
- the covariance matrix  $Q_{\xi\xi,c}$  of the process disturbance (assumed as an additive Gaussian white noise) has elements on the main diagonal equal to  $q_{cs}$  for lines in the state vector corresponding to  $c_s$  and  $q_{ce}$  for lines corresponding to  $c_e$ ; the covariance matrix  $Q_{\xi\xi,T}$  has elements on the main diagonal equal to  $q_T$  for lines in the state vector corresponding to  $T$ ;
- the covariance matrix  $R_{vv,c}$  of the measurement noise (assumed as an additive Gaussian white noise) has elements on the main diagonal equal to  $r_V$  for the line in the output vector corresponding to  $V$  and  $r_{nt}$  for the line corresponding to  $n_t$ ; the covariance matrix  $R_{vv,T}$  has elements on the main diagonal equal to  $r_T$  for the line in the output vector corresponding to  $T_{surf}$ .

Due to space limitations, only the sensitivities to a few tuning parameters are shown here. The sensitivities are presented separately for the electrochemical UKF and the thermal UKF, both with an additive noise acting on the measured variables, in order to understand the estimator robustness with respect to measurement noises and its actual filtering capability.

#### A. Tuning of the electrochemical UKF

Given the aforementioned design choices, the study of the terms in electrochemical covariance matrices follows this procedure:

- fix  $p_{cs} = 10^{-7}$ ,  $p_{ce} = 10^{-10}$  and  $p_T = 10^{-1}$ ;
- fix  $q_{ce} = 10^{-12}$  and  $q_T = 10^{-6}$ , and study sensitivity to  $q_{cs}$ ;
- fix  $r_V = 10^{-2}$ ,  $r_{nt} = 10^{-9}$  (note that, as observed in Subsection III-A,  $r_{nt} \ll r_V$ ) and  $r_T = 10^{-1}$ .

An additive noise is applied to the simulated voltage signal, according to the assumptions made above, before feeding it to UKF for the measurement-update step. The sensitivity analysis of parameter  $q_{cs}$  is performed in Figure 13.  $\varepsilon_{\text{SoC}}$  is the bulk-SoC estimation error, and is defined as the difference between the simulated and the estimated state of charge. It is used here as a synthetic figure of the electrochemical UKF accuracy, while details on local states convergence are presented in Section V. In this figure, the effect of  $q_{cs}$  on estimator convergence time is clear: the higher is  $q_{cs}$ , the lower is the time needed by UKF to converge to the true value of SoC. This time may be evaluated, for example, looking at the crossing of the level  $\varepsilon_{\text{SoC}} = 5\%$ : this goes from 180s for  $q_{cs} = 10^{-8}$

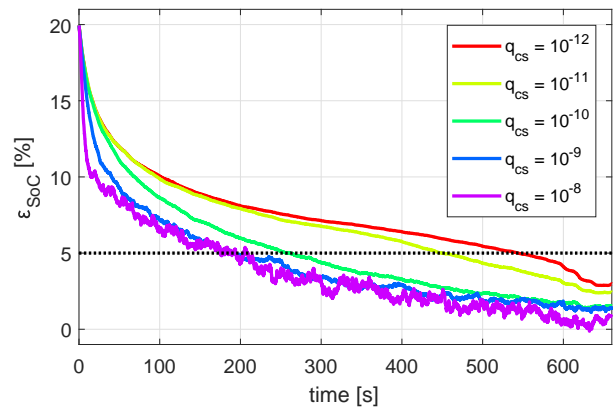


Fig. 13. Sensitivity study on parameter  $q_{cs}$ , under current input profile shown in Figure 11 and additive voltage measurement noise: differently tuned UKF estimators are entering the region at  $\varepsilon_{\text{SoC}} = 5\%$  at different time instants and show different noise rejection capability.

to 550s for  $q_{cs} = 10^{-12}$ . However, the higher is  $q_{cs}$ , the lower is also the filtering effect of UKF on measurement noise. In conclusion, a *trade-off* between convergence time and estimator rejection/filtering effect in presence of measurement noise has to be established. After extensive simulation studies, the selected values for the simulations shown in the following are  $q_{cs} = 10^{-13}$  and  $r_V = 10^{-5}$ , that will be exhaustively validated in Section V.

#### B. Tuning of the thermal UKF

The tuning study for the thermal covariance matrices has an analogous procedure:

- fix  $p_{cs} = 10^{-7}$ ,  $p_{ce} = 10^{-10}$  and  $p_T = 10^{-1}$ ;
- fix  $q_{cs} = 10^{-11}$  and  $q_{ce} = 10^{-12}$ , and study sensitivity to  $q_T$ ;
- fix  $r_V = 10^{-3}$ ,  $r_{nt} = 10^{-9}$  and  $r_T = 10^{+1}$ .

According to the assumptions above, an additive noise is applied to the simulated surface temperature signal, before feeding it to UKF for the measurement-update step. The sensitivity analysis of parameter  $q_T$  is performed in Figure 14.  $\varepsilon_{Tb}$  is the bulk temperature estimation error, and is defined as

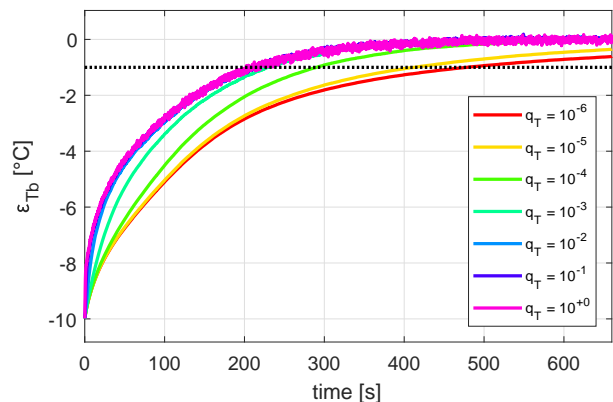


Fig. 14. Sensitivity study on parameter  $q_T$ , under current input profile shown in Figure 11 and additive surface temperature measurement noise: differently tuned UKF estimators are entering the region at  $\varepsilon_{Tb} = -1^\circ\text{C}$  at different time instants and show different noise rejection capability.

the difference between the simulated and the estimated bulk temperature. It is used here as a synthetic figure of the thermal UKF accuracy, while details on local states convergence are presented in Section V. The effect of  $q_T$  on estimator convergence time is evident from the figure: the higher is  $q_T$ , the lower is the time needed by UKF to converge to the true value of  $T_{bulk}$ . For example, looking at the crossing of the level  $\varepsilon_{Tb} = -1^\circ\text{C}$ , the convergence time goes from 200s for  $q_T = 10^{+0}$  to 500s for  $q_T = 10^{-6}$ . However, the higher is  $q_T$ , the lower is also the noise filtering effect of UKF. In all considered cases, the estimator is able to fully recover from wrong initialization. In conclusion, a similar *trade-off* as for the electrochemical UKF needs to be settled. After extensive simulation studies, the selected values used in the following are  $q_T = 10^{-6}$  and  $r_T = 10^{-1}$ , which will be thoroughly validated in the next section.

## V. VALIDATION

This section validates first the soft-constrained DUKF in two different scenarios. Then, the advantages of the dual observer structure are detailed and analyzed in Subsection V-A. All the simulation results presented hereafter are obtained by relying on a coupled electrochemical-thermal model, solved via an ODE solver in MATLAB environment, as explained in [25].

The tests designed for validation purposes are both with noisy voltage and surface temperature measurements. They are defined as follows:

- 1) The current pulses profile at 10C introduced in Subsection III-B and depicted in Figure 11.
- 2) A more dynamic test, consisting of a repeating sequence of current pulses, both positive and negative, with increasing amplitude (as high as 50C or 300A), as shown in Figure 15; the simulator starts at  $\text{SoC} = 100\%$  and  $T = 10^\circ\text{C}$  (to simulate a cooling system), and the pulses are designed so that the cell is overall discharging during the test. As before, the simulation is stopped when  $V$  reaches 2.7V.

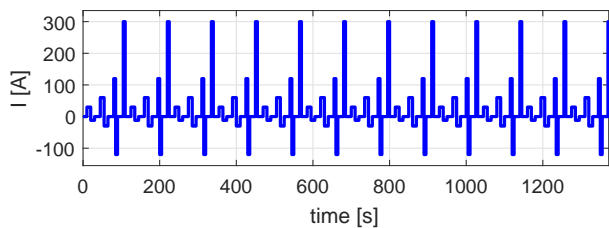


Fig. 15. Current input profile used to validate the DUKF: sequence of pulses at increasing amplitude (5C-10C-20C-50C in discharge).

The estimator convergence results for the bulk SoC in the first test are presented in Figure 16; both SoC and  $\varepsilon_{\text{SoC}}$  are expressed in percentage. The DUKF is initialized at different initial guesses of SoC and  $T_{bulk}$ , indicated as  $\text{SoC}_{0,\text{UKF}}$  and  $T_{0,\text{UKF}}$ , respectively. Also, convergence results for bulk temperature are shown in Figure 17. Temperatures are expressed in degrees Celsius. It is confirmed that, even in the presence of noisy measured signals:

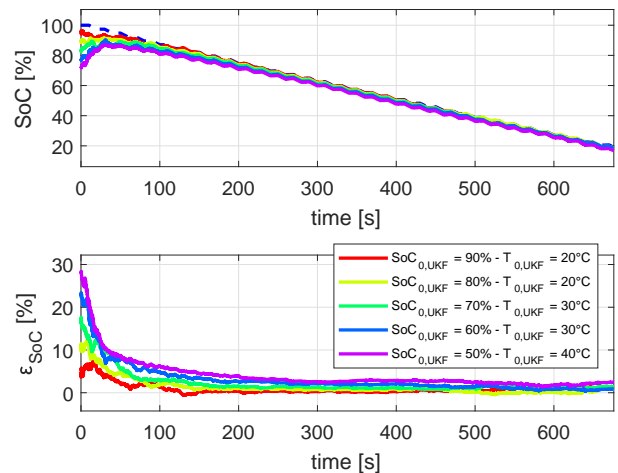


Fig. 16. Bulk SoC estimation results for the first scenario, with several values of  $\text{SoC}_{0,\text{UKF}}$  and  $T_{0,\text{UKF}}$ : for all values of initialization, the estimator converges on the true SoC value.

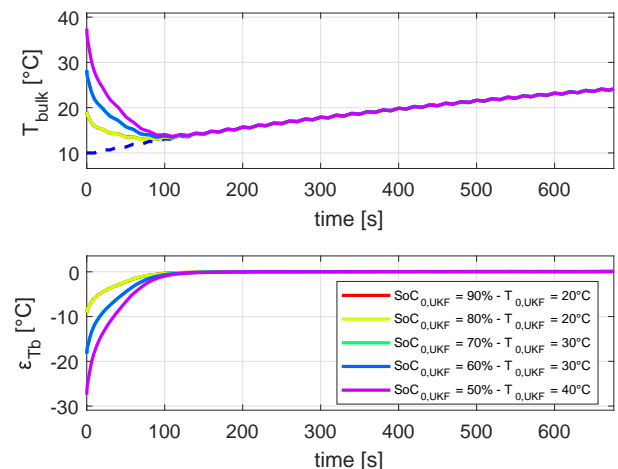


Fig. 17. Bulk temperature estimation results for the first scenario, with several values of  $\text{SoC}_{0,\text{UKF}}$  and  $T_{0,\text{UKF}}$ : for all values of initialization, the estimator converges on the true  $T_{bulk}$  value.

- The estimator is robust enough to recover and finally converge to the true value of SoC and  $T_{bulk}$  even for a large initialization error in both the electrochemical and thermal parts, respectively of up to 50% and up to  $30^\circ\text{C}$ .
- The initial convergence rate is very fast, for all considered initializations: the SoC error goes below 10% in less than 40s, while the bulk temperature error goes below  $5^\circ\text{C}$  (in absolute value) in less than 60s.
- After the initial transient (roughly 250s), the SoC error keeps always under 3% (in absolute value), and reaches values as low as 1.5% by the end of the test in all cases apart ( $\text{SoC}_{0,\text{UKF}} = 50\%$ ,  $T_{0,\text{UKF}} = 40^\circ\text{C}$ ); the bulk temperature error is always below  $0.1^\circ\text{C}$  (in absolute value) after the initial transient.

Furthermore, Figure 18 and Figure 19 plot the estimation of lithium concentration distributions in solid phase at different time instants. The former figure plots the estimation of surface stoichiometry for all spherical particles along  $x$ , while the latter figure plots the estimation of stoichiometry along the

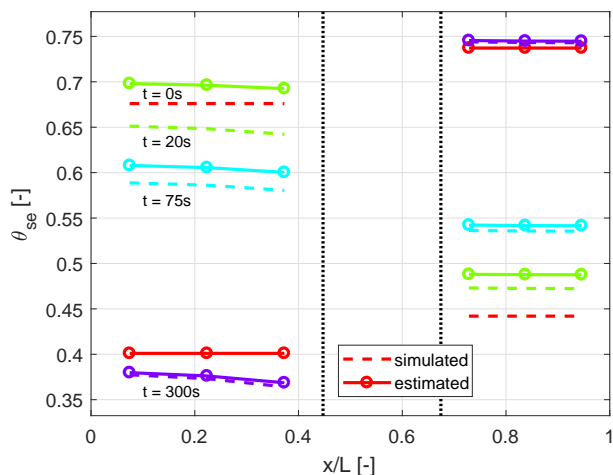


Fig. 18. Surface stoichiometry distribution along  $x$  direction, at different time instants (depicted with different colors) for the first scenario. Vertical dotted lines indicate the separation among domains: negative electrode (left), separator (center) and positive electrode (right).

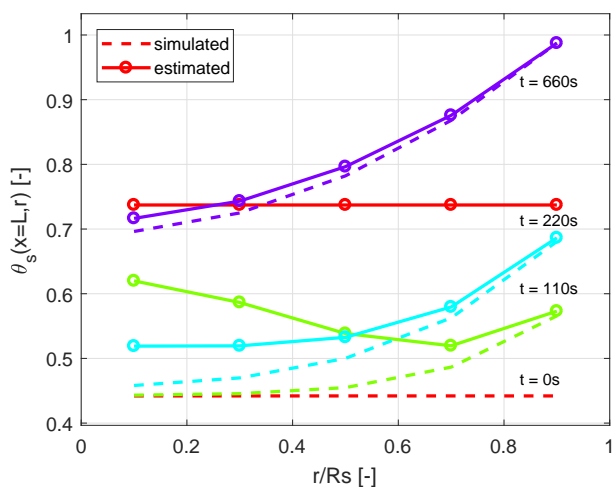


Fig. 19. Stoichiometry distribution along  $r$  direction of the spherical particle at  $x = L$ , at different time instants (depicted with different colors) for the first scenario.

radial direction of a spherical particle close to the positive current collector. In both cases, the DUKF converges to the true continuous value of concentrations and accurately estimates the gradients. Note that, in Figure 18, the convergence of positive electrode states is faster than negative electrode ones, due to model parameterization and filter tuning. From Figure 19, it is clear how surface stoichiometry has a faster convergence over the core one, because the former is the one more directly affecting the measured voltage. Also, close to the end of simulation, as can be seen, for example, at  $t = 660s$ , values of surface stoichiometry are reached that are close to active material saturation/depletion; in these conditions, the thermodynamic equilibrium potential  $U$  exhibits a strong non-linear dependency on  $\theta_{se}$ . The DUKF observer is effectively capable of capturing this non-linearity. Finally, Figure 20 shows the temperature distribution in the cylindrical cell at several time instants. From the figure, it can be seen that the surface temperature is converging close to the true value in

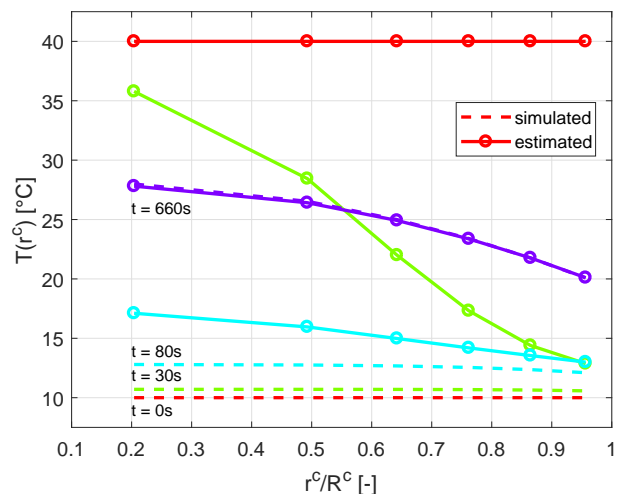


Fig. 20. Temperature distribution along  $r^c$  direction of the cylindrical cell, at different time instants (depicted with different colors) for the first scenario.

the first seconds of the test, because it is a measured quantity; on the contrary, the convergence of the core temperature requires more time. At the end of the test a gradient of about  $7.5^\circ\text{C}$  is generated between the surface and the core, with the latter being warmer. This gradient is correctly captured by the DUKF.

The proposed dual observer is able to estimate both the bulk SoC and the concentration gradients, as well as the temperature distribution, also in the second scenario, that encompasses a more demanding input. The same representation used above is followed by Figures 21-25. As before, the

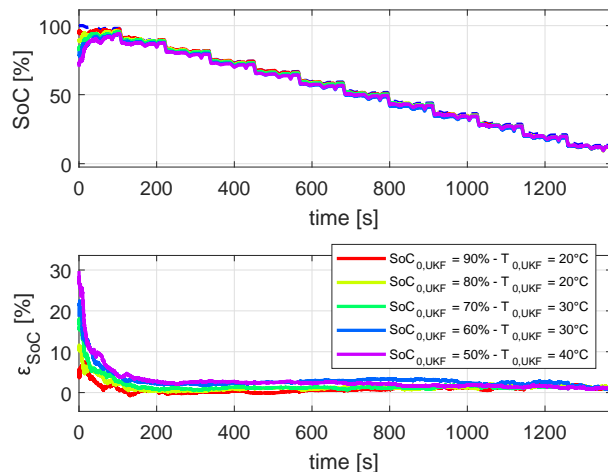


Fig. 21. Bulk SoC estimation results for the second scenario, with several values of  $\text{SoC}_{0,\text{UKF}}$  and  $T_{0,\text{UKF}}$ : for all values of initialization, the estimator converges on the true SoC value.

DUKF estimator is very robust to noisy measurements and large initial estimation error (of up to 50% and  $30^\circ\text{C}$ ).  $\epsilon_{\text{SoC}}$  converges in all cases to values below 3.5% (in absolute value) in less than 200s, and below roughly 1.5% by the end of the test. The same convergence rate is observed in the estimation of solid particles surface and inner lithium concentrations.  $\epsilon_{T_b}$  converges in all cases to values below  $0.5^\circ\text{C}$  (in absolute value) in less than 120s, and similar results are obtained

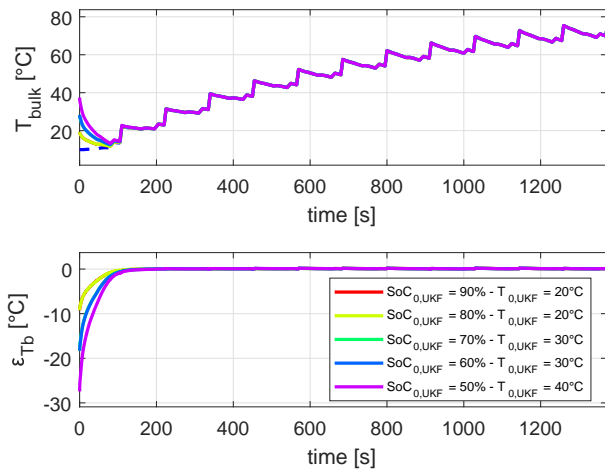


Fig. 22. Bulk temperature estimation results for the second scenario, with several values of  $SoC_{0,UKF}$  and  $T_{0,UKF}$ : for all values of initialization, the estimator converges on the true  $T_{bulk}$  value.

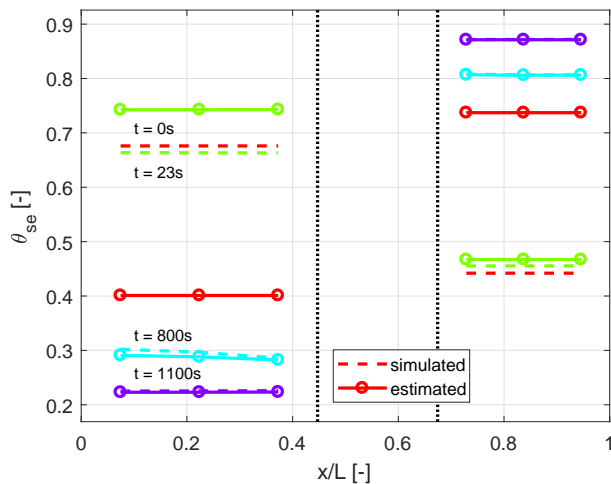


Fig. 23. Surface stoichiometry distribution along  $x$  direction, at different time instants (depicted with different colors) for the second scenario. Vertical dotted lines indicate the separation among domains: negative electrode (left), separator (center) and positive electrode (right).

for the whole temperature profile along the radius. It is important to note that, in these conditions with higher currents, greater internal gradients are triggered, both for concentrations and temperatures; as such, estimating these gradients is even more important here. For example, the temperature difference between the surface and the core of the cell assumes the substantial value of  $35^{\circ}C$  towards the end of the test. Also in this case, DUKF estimator is capable to overcome the high non-linearity due to extreme values of surface concentrations reached in the final part of the test (see for example Figure 24 for  $t = 1030s$ ).

#### A. Remark on observer dual structure

This subsection further illustrate the advantages of the dual structure. The analysis shows that joint temperature and chemical dynamics estimation is required for accurate results; at the same time, the analysis exemplifies how the DUKF structure

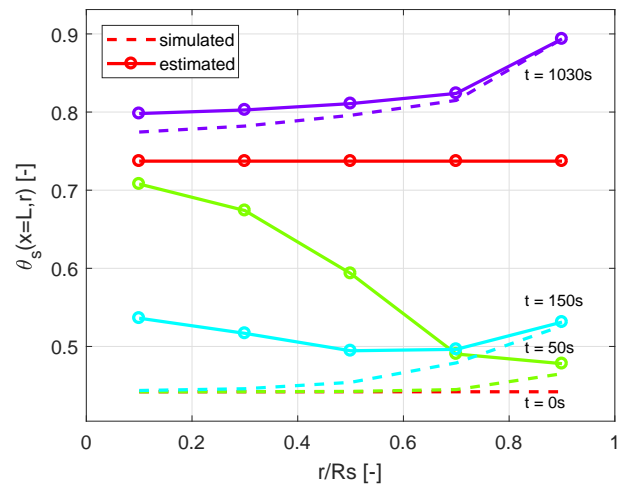


Fig. 24. Stoichiometry distribution along  $r$  direction of the spherical particle at  $x = L$ , at different time instants (depicted with different colors) for the second scenario.

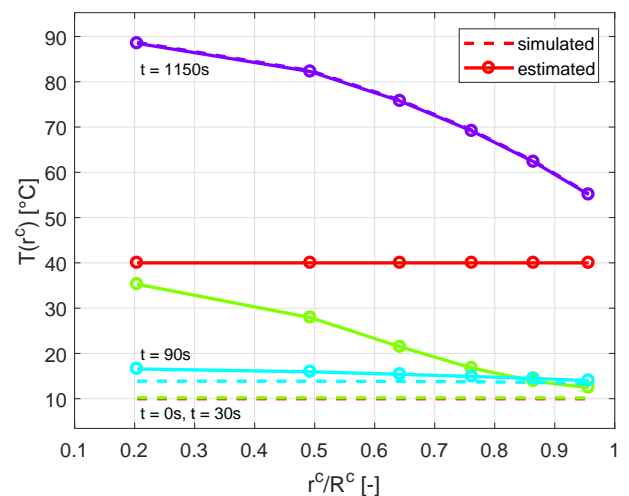


Fig. 25. Temperature distribution along  $r^c$  direction of the cylindrical cell, at different time instants (depicted with different colors) for the second scenario.

achieves this result with a limited increase in complexity with respect to chemical dynamic only estimators.

Consider the electrochemical UKF subject to the input current of Figure 15, and initialized with 20% initial SoC error. The simulated temperature profiles from the coupled electrochemical-thermal model, with  $N_c = 6$ , are shown in Figure 26, for the surface and core subcells. Note that the simulator is initialized at  $T = 10^{\circ}C$ . In this study, the

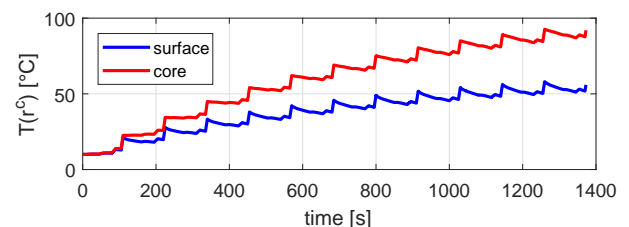


Fig. 26. Simulated temperature profiles at surface and core of the cell, under the same current of Figure 15.

electrochemical UKF is run with three different temperature inputs: (i) a constant temperature equal to  $T_{ref}$ , which is equivalent to fix P2D model parameters to their nominal value, as if there were no temperature measurement available (see (5)); (ii) a wrong constant temperature measurement, namely  $T = 10^\circ\text{C}$ , that is the initial cell temperature in the simulated test, as if there were no thermal dynamics leading to an overall increase of temperatures; (iii) a bulk temperature measurement, computed from simulated temperature states via (12). The observer states estimation results can be compared to the simulated concentrations from the coupled electrochemical-thermal model by looking at Figure 27. Recalling the final

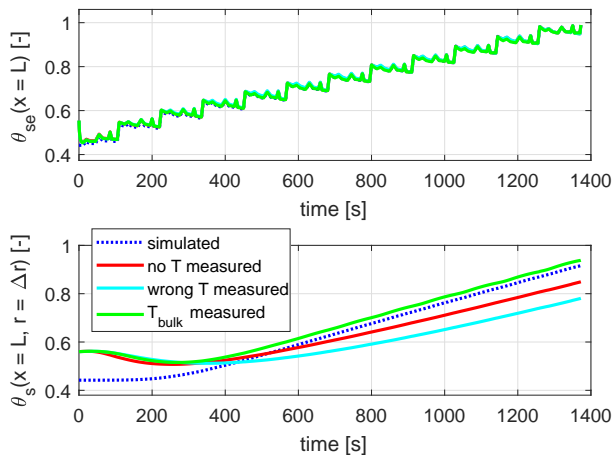


Fig. 27. Solid phase stoichiometry at surface (top) and core (bottom) of the particle located close to positive electrode current collector, under the current profile of Figure 15. Simulated results from the coupled electrochemical-thermal model are compared to estimations from the electrochemical UKF. Three different temperature measurements are considered for the observer.

objective of the present work, that is the estimation of local values of lithium concentrations and of temperatures, from the figures above two conclusions can be drawn, which confirm the literature results reported in Section I:

- 1) Lithium concentrations estimation is strongly affected by thermal dynamics. In fact, while surface stoichiometry is estimated at an acceptable accuracy level in all considered cases (recall that the surface stoichiometry is the one more directly affecting the measured variable  $V$ ), the core stoichiometry is not correctly estimated by the electrochemical UKF that does not receive *at least* a bulk temperature measurement. Without such a measurement, the estimated core stoichiometry exhibits an error as large as 15% of the simulated value.
- 2) The estimation of local temperatures, and in particular of core temperature, is not a minor task, but is critical for the cell safety and performances. At the end of the considered test, while the surface temperature (measurable quantity) is still at about  $50^\circ\text{C}$ , which may be below the recommended maximum temperature for a standard production cell, the core temperature reaches a temperature of  $95^\circ\text{C}$ , which is surely detrimental and possibly dangerous for most Li-ion cells. As such, an estimate of temperatures distribution inside the cell is necessary, and a simple bulk temperature estimation

may not be enough to detect a thermal runaway under demanding input currents.

## VI. CONCLUSIONS

In the present work, a DUKF observer is applied to an electrochemical-thermal model of a Li-ion cell, composed of the complete P2D model and a distributed thermal model. The P2D model represents a good trade-off between electrochemical modeling complexity and accuracy. The goal is that of estimating both the bulk SoC and the lithium concentration distribution in the solid phase, as well as both the bulk temperature and the temperature distribution in the cell. Observing the internal states of the electrochemical model is particularly challenging because of convergence issues of the estimate of lithium concentration in solid phase. In this work, the issues are solved by introducing a soft-constraint in the DUKF implementation.

Using Unscented Kalman Filtering in this problem has several advantages: it overcomes the high non-linearity of the electrochemical model; it provides tools for a simple integration of the additional lithium mass conservation constraint; it is amenable to parallel implementation; and it guarantees a fast and robust convergence from large initial estimation errors. In addition, the proposed dual structure augments the description capability and accuracy of a previously proposed UKF observer by the same authors of this paper, making use of a minimal set of information.

An extensive validation campaign eventually confirms the ability of the novel approach to estimate accurately both bulk quantities, such as SoC and  $T_{bulk}$ , and local concentration and temperature values in any point of the cell.

## ACKNOWLEDGMENTS

This work was supported by Ministero dell’Istruzione, dell’Università e della Ricerca SIR project RBSI14STHV.

## REFERENCES

- [1] Y. Wang, H. Fang, L. Zhou, and T. Wada, “Revisiting the state-of-charge estimation for lithium-ion batteries: A methodical investigation of the extended kalman filter approach,” *IEEE Control Systems Magazine*, vol. 37, no. 4, pp. 73–96, Aug 2017.
- [2] K. B. Hatzell, A. Sharma, and H. K. Fathy, “A survey of long-term health modeling, estimation, and control of lithium-ion batteries: Challenges and opportunities,” in *American Control Conference (ACC), 2012*. IEEE, 2012, pp. 584–591.
- [3] K. Somasundaram, E. Birgersson, and A. S. Mujumdar, “Thermal-electrochemical model for passive thermal management of a spiral-wound lithium-ion battery,” *Journal of Power Sources*, vol. 203, pp. 84–96, 2012.
- [4] N. A. Chaturvedi, R. Klein, J. Christensen, J. Ahmed, and A. Kojic, “Algorithms for advanced battery-management systems,” *IEEE Control Systems*, vol. 30, no. 3, pp. 49–68, 2010.
- [5] P. W. Northrop, B. Suthar, V. Ramadesigan, S. Santhanagopalan, R. D. Braatz, and V. R. Subramanian, “Efficient simulation and reformulation of lithium-ion battery models for enabling electric transportation,” *Journal of The Electrochemical Society*, vol. 161, no. 8, pp. E3149–E3157, 2014.
- [6] L. Gao, S. Liu, and R. A. Dougal, “Dynamic lithium-ion battery model for system simulation,” *IEEE Transactions on Components and Packaging Technologies*, vol. 25, no. 3, pp. 495–505, Sep 2002.
- [7] R. C. Kroeze and P. T. Krein, “Electrical battery model for use in dynamic electric vehicle simulations,” in *2008 IEEE Power Electronics Specialists Conference*, June 2008, pp. 1336–1342.

- [8] M. Corno and S. M. Savaresi, "A diffusive electro-equivalent li-ion battery model," in *Circuits and Systems (ISCAS), 2013 IEEE International Symposium on*. IEEE, 2013, pp. 2976–2979.
- [9] S. Santhanagopalan, Q. Guo, P. Ramadass, and R. E. White, "Review of models for predicting the cycling performance of lithium ion batteries," *Journal of Power Sources*, vol. 156, no. 2, pp. 620–628, 2006.
- [10] C. Wang and V. Srinivasan, "Computational battery dynamics (cbd)electrochemical/thermal coupled modeling and multi-scale modeling," *Journal of power sources*, vol. 110, no. 2, pp. 364–376, 2002.
- [11] G. G. Botte, V. R. Subramanian, and R. E. White, "Mathematical modeling of secondary lithium batteries," *Electrochimica Acta*, vol. 45, no. 15, pp. 2595–2609, 2000.
- [12] C. Forgez, D. V. Do, G. Friedrich, M. Morcrette, and C. Delacourt, "Thermal modeling of a cylindrical lifepo4/graphite lithium-ion battery," *Journal of Power Sources*, vol. 195, no. 9, pp. 2961–2968, 2010.
- [13] K. A. Smith, C. D. Rahn, and C. Y. Wang, "Model-based electrochemical estimation and constraint management for pulse operation of lithium ion batteries," *IEEE Transactions on Control Systems Technology*, vol. 18, no. 3, pp. 654–663, May 2010.
- [14] K. Smith and C.-Y. Wang, "Power and thermal characterization of a lithium-ion battery pack for hybrid-electric vehicles," *Journal of power sources*, vol. 160, no. 1, pp. 662–673, 2006.
- [15] Q. Wang, P. Ping, X. Zhao, G. Chu, J. Sun, and C. Chen, "Thermal runaway caused fire and explosion of lithium ion battery," *Journal of Power Sources*, vol. 208, pp. 210 – 224, 2012.
- [16] M. Doyle, T. F. Fuller, and J. Newman, "Modeling of galvanostatic charge and discharge of the lithium/polymer/insertion cell," *Journal of the Electrochemical Society*, vol. 140, no. 6, pp. 1526–1533, 1993.
- [17] K. Smith and C.-Y. Wang, "Solid-state diffusion limitations on pulse operation of a lithium ion cell for hybrid electric vehicles," *Journal of Power Sources*, vol. 161, no. 1, pp. 628–639, 2006.
- [18] K. A. Smith, C. D. Rahn, and C.-Y. Wang, "Control oriented 1d electrochemical model of lithium ion battery," *Energy Conversion and management*, vol. 48, no. 9, pp. 2565–2578, 2007.
- [19] A. M. Bizeray, S. Zhao, S. R. Duncan, and D. A. Howey, "Lithium-ion battery thermal-electrochemical model-based state estimation using orthogonal collocation and a modified extended kalman filter," *Journal of Power Sources*, vol. 296, pp. 400–412, 2015.
- [20] J. C. Forman, S. J. Moura, J. L. Stein, and H. K. Fathy, "Genetic parameter identification of the doyle-fuller-newman model from experimental cycling of a lifepo 4 battery," in *American Control Conference (ACC), 2011*. IEEE, 2011, pp. 362–369.
- [21] V. Ramadesigan, V. Boovaragavan, J. C. Pirkle, and V. R. Subramanian, "Efficient reformulation of solid-phase diffusion in physics-based lithium-ion battery models," *Journal of The Electrochemical Society*, vol. 157, no. 7, pp. A854–A860, 2010.
- [22] J. C. Forman, S. Bashash, J. L. Stein, and H. K. Fathy, "Reduction of an electrochemistry-based li-ion battery model via quasi-linearization and pade approximation," *Journal of the Electrochemical Society*, vol. 158, no. 2, pp. A93–A101, 2011.
- [23] P. P. Mishra, M. Garg, S. Mendoza, J. Liu, C. D. Rahn, and H. K. Fathy, "How does model reduction affect lithium-ion battery state of charge estimation errors? theory and experiments," *Journal of The Electrochemical Society*, vol. 164, no. 2, pp. A237–A251, 2017.
- [24] V. R. Subramanian, V. D. Diwakar, and D. Tapriyal, "Efficient macro-micro scale coupled modeling of batteries," *Journal of The Electrochemical Society*, vol. 152, no. 10, pp. A2002–A2008, 2005.
- [25] L. Onesto, S. Marelli, and M. Corno, "Control-oriented coupled electrochemical thermal model for li-ion batteries," in *2017 IEEE 56th Annual Conference on Decision and Control (CDC), 2017*, pp. 5026–5031.
- [26] B. Wang, Z. Liu, S. E. Li, S. J. Moura, and H. Peng, "State-of-charge estimation for lithium-ion batteries based on a nonlinear fractional model," *IEEE Transactions on Control Systems Technology*, vol. 25, no. 1, pp. 3–11, 2017.
- [27] S. J. Moura, N. A. Chaturvedi, and M. Krstic, "Pde estimation techniques for advanced battery management systems, part i: Soc estimation," in *American Control Conference (ACC), 2012*. IEEE, 2012, pp. 559–565.
- [28] N. Lotfi, R. G. Landers, J. Li, and J. Park, "Reduced-order electrochemical model-based soc observer with output model uncertainty estimation," *IEEE Transactions on Control Systems Technology*, vol. 25, pp. 1217–1230, 2017.
- [29] M. Corno, N. Bhatt, S. M. Savaresi, and M. Verhaegen, "Electrochemical model-based state of charge estimation for li-ion cells," *IEEE Transactions on Control Systems Technology*, vol. 23, no. 1, pp. 117–127, 2015.
- [30] S. J. Julier, J. K. Uhlmann, and H. F. Durrant-Whyte, "A new approach for filtering nonlinear systems," in *American Control Conference, Proceedings of the 1995*, vol. 3, Jun 1995, pp. 1628–1632 vol.3.
- [31] G. L. Plett, "Sigma-point kalman filtering for battery management systems of lipb-based hev battery packs: Part 1: Introduction and state estimation," *Journal of Power Sources*, vol. 161, no. 2, pp. 1356–1368, 2006.
- [32] S. Santhanagopalan and R. E. White, "State of charge estimation using an unscented filter for high power lithium ion cells," *International Journal of Energy Research*, vol. 34, no. 2, pp. 152–163, 2010.
- [33] S. Marelli and M. Corno, "A soft-constrained unscented kalman filter estimator for li-ion cells electrochemical model," in *2017 IEEE 56th Annual Conference on Decision and Control (CDC), 2017*, pp. 1535–1540.
- [34] G. L. Plett, "Sigma-point kalman filtering for battery management systems of lipb-based hev battery packs: Part 2: Simultaneous state and parameter estimation," *Journal of power sources*, vol. 161, no. 2, pp. 1369–1384, 2006.
- [35] J. L. Crassidis and F. L. Markley, "Unscented filtering for spacecraft attitude estimation," *Journal of Guidance Control and Dynamics*, vol. 26, no. 4, pp. 536–542, 2003.
- [36] S. Al Hallaj, H. Maleki, J.-S. Hong, and J. R. Selman, "Thermal modeling and design considerations of lithium-ion batteries," *Journal of Power Sources*, vol. 83, no. 1, pp. 1–8, 1999.
- [37] T. Evans and R. E. White, "A thermal analysis of a spirally wound battery using a simple mathematical model," *Journal of The Electrochemical Society*, vol. 136, no. 8, pp. 2145–2152, 1989.
- [38] S. Anwar, C. Zou, and C. Manzie, "Distributed thermal-electrochemical modeling of a lithium-ion battery to study the effect of high charging rates," *IFAC Proceedings Volumes*, vol. 47, no. 3, pp. 6258–6263, 2014.
- [39] Y. Kim, J. B. Siegel, and A. G. Stefanopoulou, "A computationally efficient thermal model of cylindrical battery cells for the estimation of radially distributed temperatures," pp. 698–703, 2013.
- [40] E. A. Wan and R. V. D. Merwe, "The unscented kalman filter for nonlinear estimation," in *Proceedings of the IEEE 2000 Adaptive Systems for Signal Processing, Communications, and Control Symposium (Cat. No.00EX373)*, 2000, pp. 153–158.
- [41] D. Di Domenico, A. Stefanopoulou, and G. Fiengo, "Lithium-ion battery state of charge and critical surface charge estimation using an electrochemical model-based extended kalman filter," *Journal of dynamic systems, measurement, and control*, vol. 132, no. 6, p. 061302, 2010.
- [42] A. Bartlett, J. Marcicki, S. Onori, G. Rizzoni, X. G. Yang, and T. Miller, "Electrochemical model-based state of charge and capacity estimation for a composite electrode lithium-ion battery," *IEEE Transactions on Control Systems Technology*, vol. 24, no. 2, pp. 384–399, 2016.